

DOI: 10.1002/adem.201400136

# Advanced Scale Bridging Microstructure Analysis of Single Crystal Ni-Base Superalloys<sup>\*\*</sup>

By Alireza B. Parsa,\* Philip Wollgramm, Hinrich Buck, Christoph Somsen, Aleksander Kostka, Ivan Povstugar, Pyuck-Pa Choi, Dierk Raabe, Antonin Dlouhy, Julian Müller, Erdmann Spiecker, Kathrin Demtroder, Jürgen Schreuer, Klaus Neuking and Gunther Eggeler

*In the present work, we show how conventional and advanced mechanical, chemical, and microstructural methods can be used to characterize cast single crystal Ni-base superalloy (SX) plates across multiple length scales. Two types of microstructural heterogeneities are important, associated with the cast microstructure (dendrites (D) and interdendritic (ID) regions – large scale heterogeneity) and with the well-known  $\gamma/\gamma'$  microstructure (small scale heterogeneity). Using electron probe microanalysis (EPMA), we can show that elements such as Re, Co, and Cr partition to the dendrites while ID regions contain more Al, Ta, and Ti. Analytical transmission electron microscopy and atom probe tomography (APT) show that Al, Ta, and Ti partition to the  $\gamma'$  cubes while  $\gamma$  channels show higher concentrations of Co, Cr, Re, and W. We can combine large scale (EPMA) and small-scale analytical methods (APT) to obtain reasonable estimates for  $\gamma'$  volume fractions in the dendrites and in the ID regions. The chemical and mechanical properties of the SX plates studied in the present work are homogeneous, when they are determined from volumes with dimensions, which are significantly larger than the dendrite spacing. For the SX plates (140 mm  $\times$  100 mm  $\times$  20 mm) studied in the present work this holds for the average chemical composition as well as for elastic behavior and local creep properties. We highlight the potential of HRTEM and APT to contribute to a better understanding of the role of dislocations during coarsening of the  $\gamma'$  phase and the effect of cooling rates after high temperature exposure on the microstructure.*

## 1. Introduction

Ni-base single crystal superalloys (SXs) are used to make first stage blades in gas turbines for energy production and aero engines, which operate at temperatures above 1000 °C.<sup>[1,2]</sup> They are produced by combining vacuum induction melting with a Bridgman type of solidification process and require subsequent multiple step heat treatments. A modified

Bridgman process with a grain selector is used to exploit dendritic solidification to produce single crystals.<sup>[1–7]</sup>

Three types of heterogeneities characterize technical Ni-base SXs. The first category consists of casting defects like interfaces, freckles, and pores.<sup>[4–6]</sup> The second category of heterogeneities is related to the cast microstructure, which is governed by the growth of dendrites (D) and the subsequent

[\*] A. B. Parsa, P. Wollgramm, H. Buck, C. Somsen, K. Neuking, G. Eggeler  
Institut für Werkstoffe, Ruhr-Universität Bochum, Universitätstr. 150, 44780 Bochum, Germany  
E-mail: alireza.basirparsa@rub.de  
A. Kostka, I. Povstugar, P.-P. Choi, D. Raabe  
Max-Planck-Institut für Eisenforschung, Max Planck Str. 1, 40237 Dusseldorf, Germany  
A. Dlouhy  
Institute of Physics of Materials, Žitkova 22, Brno, Czech Republic

J. Müller, E. Spiecker  
Center for Nanoanalysis and Electron Microscopy, Friedrich-Alexander Universität Erlangen-Nürnberg, Cauerstr. 6, Erlangen, Germany  
K. Demtroder, J. Schreuer  
Institut für Geowissenschaften, Ruhr-Universität Bochum, Universitätstr. 150, 44780 Bochum, Germany

[\*\*] A. B. P. acknowledges funding through the International Max Planck Research School (IMPRS) on Surface and Interface Engineering of Advanced Materials (SurMat). All authors acknowledge funding by the German Research Association (DFG) through projects A1, A2, A4, and A7 of the collaborative research center SFB/TR 103.

solidification of interdendritic (ID) regions.<sup>[4–7]</sup> The chemical composition of the D and ID regions after solidification differs and a homogenization heat treatment is required to achieve a homogeneous chemical composition.<sup>[4–7]</sup> During solidification of Ni-base superalloys, large  $\gamma'$  particles form. These do not contribute to good creep strength and need to be dissolved. However, their dissolution temperature,  $T_{\text{diss}}$ , can be higher than the melting point of the as cast ID regions,  $T_{\text{M-ID}}^0$ . Both temperatures are indicated as horizontal dotted lines in Figure 1, where the heat treatment temperature is plotted as a function of exposure time. A successful heat treatment must start at  $T_1$ , just below the melting point of the as cast ID regions, Figure 1. During the hold time at  $T_1$  (typically 1–2 h), interdiffusion processes between D and ID occur. As the ID regions adjust their composition, their melting point  $T_{\text{M-ID}}$  gradually increases, as indicated by the dashed line in Figure 1. This eventually allows to safely apply the next heat treatment step at  $T_2$ , and, after an appropriate hold time,  $T_3$  and so on. During this type of multiple step homogenization heat treatment (in the example of Figure 1:  $T_1 \rightarrow T_2 \rightarrow T_3 \rightarrow T_4$ ), the melting of ID regions is avoided. If it occurs, it represents a processing issue, which is referred to as incipient melting.<sup>[4–6]</sup> As schematically illustrated in Figure 1, a successful multiple step heat treatment approaches the dissolution limit  $T_{\text{diss}}$  of the large  $\gamma'$  particles from below without ever surpassing the actual melting point of the ID regions. After full homogenization, the material is cooled down to  $T_{\text{prec}}$ , where the well-known  $\gamma/\gamma'$  microstructure forms. It consists of small  $\gamma'$  cubes (ordered  $\text{L}_{12}$  crystal structure, typical cube edge length: 0.3–0.8  $\mu\text{m}$ , typical  $\gamma'$  volume fraction: between 60 and 80%) separated by thin  $\gamma$  channels (fcc crystal structure, typical  $\gamma$  channel width: 40–100 nm, typical  $\gamma$  volume fraction between 20 and 40%).<sup>[5–11]</sup> The two phase microstructure consisting of  $\gamma'$  cubes separated by thin  $\gamma$  channels represents the well-known small scale heterogeneity (length scale: 1  $\mu\text{m}$ ) which characterizes the microstructure of all single crystal superalloys.

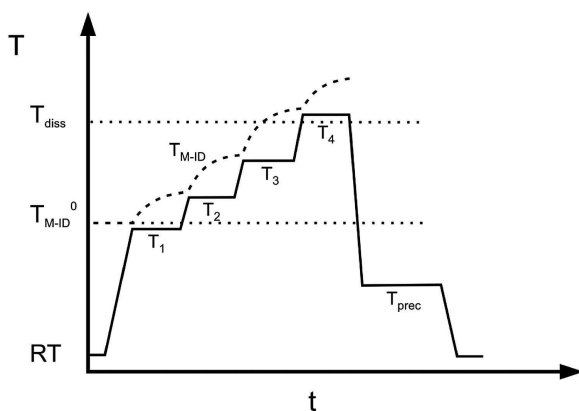


Fig. 1. Schematic temperature ( $T$ ) time ( $t$ ) chart illustrating the multiple step heat treatment of a single crystal superalloy.  $T_{\text{M-ID}}$  is the melting point of the interdendritic region ( $T_{\text{M-ID}}^0$  for  $t = 0$ ),  $T_1$ – $T_4$  are temperature steps taken to avoid reaching  $T_{\text{M-ID}}$ .  $T_{\text{diss}}$  is the temperature at which initial  $\gamma'$  cubes dissolve and  $T_{\text{prec}}$  is the temperature where the small  $\gamma'$  cubes, which provide creep strength precipitate, RT, room temperature.

From a fundamental point of view, there is no reason why full chemical homogeneity could not be achieved. However, in SX technology, it is important to keep the duration of heat treatments short, not only to keep processing costs at a minimum, but also to limit chemical and metallurgical reactions, which can occur during long-term high temperature exposure (e.g., oxidation and other reactions with the environment). As a consequence chemical equilibrium is hardly ever achieved and it is quite common to find chemical and microstructural differences between D and ID regions.

In the present study, we document the chemical, microstructural, and mechanical characterization of SX plates with compositions similar to CMSX-4 alloy. To this end we use optical microscopy (OM), advanced scanning electron microscopy (SEM), electron probe microanalysis (EPMA), analytical transmission electron microscopy (TEM), high resolution transmission electron microscopy (HRTEM), and atom probe tomography (APT) to characterize and discuss chemical and microstructural heterogeneities in Ni-base SX superalloys on different length scales. Moreover, we characterize the homogeneity of a typical laboratory plate with respect to average chemical composition, elastic constants, and local creep properties. We show how conventional and advanced characterization methods can be combined to contribute to a better understanding of the microstructure of SX Ni-base superalloys.

## 2. Experiments

### 2.1. Alloy Composition, Single Crystalline Plates, and Heat Treatment

Ni-base superalloys are multicomponent systems, which contain up to 10 major alloying elements. The composition of the alloy ERBO/1 is shown in Table 1. It is an alloy of type CMSX-4. The master melt was provided by Cannon-Muskegon. It was cast into single crystal plates some of which were investigated in the as cast conditions and others were heat treated, following a specific heat treatment by Doncasters Precision Casting, Bochum. Table 1 shows the as specified chemical composition of the material. The objective of the present work is to characterize microstructural and chemical features of typical single crystal laboratory plates in the as cast (ERBO/1A-1) and fully heat-treated (ERBO/1C-1) condition (alloy designations see Appendix 1).

In the present work, we investigate cast plates like the one shown in Figure 2a and b. We assess the chemical homogeneity of such a plate, in order to provide information on representative local chemical, microstructural, and mechanical properties. The material investigated in the present study was cast in the shape of plates, Figure 2. Figure 2a shows a photograph of a plate (140 mm  $\times$  100 mm  $\times$  20 mm). Figure 2b shows a schematic drawing of the plate together with a reference coordinate system  $x$ ,  $y$ , and  $z$ . The nominal [001] solidification direction is parallel to the  $z$ -axis. Figure 2b represents a cut up plan, which identifies specific segments A1, A2, A3, B1, ..., E3. Chemical data were obtained from the

Table 1. Chemical composition of alloys ERBO/1 as specified prior to melting.

Element [wt%]	Al	Co	Cr	Hf	Mo	Re	Ta	Ti	W	Ni
As specified	5.4–5.75	9.3–10.0	6.2–6.6	0.07–0.12	0.5–0.7	2.8–3.1	6.3–6.75	0.9–1.1	6.2–6.6	Bal.

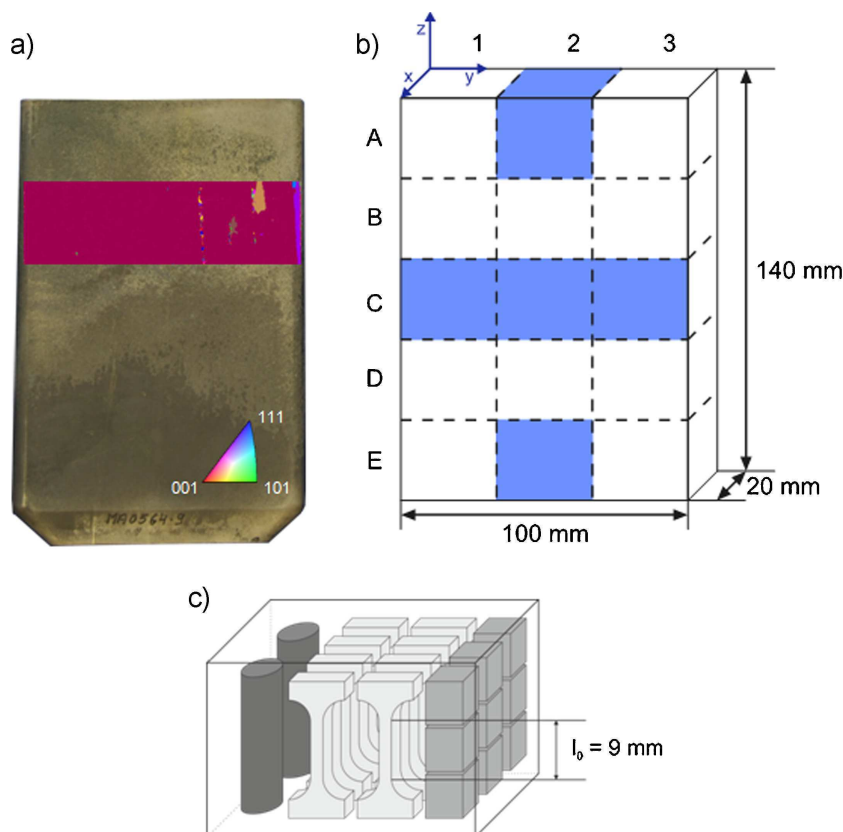


Fig. 2. As cast SX plate ERBO/1A-1/9 investigated in the present study. (a) Photograph of the plate together with color-coded EBSD results. (b) Dimensions of the cast plate and xyz coordinate system. Solidification occurred in z-direction. The cut up plan identifies specific plate segments referred to as A1, A2, A3, B1, ..., E3. (c) Schematic illustration showing how specific specimens were taken from one plate segment (vertical edge parallel).<sup>[1]</sup> Light gray: miniature creep specimens (the 9 mm gauge length of one creep specimen is indicated), middle gray: rectangular parallelepipeds as used in for elastic constant measurements.

Revierlabor, Essen, where X-ray fluorescence spectroscopy (XRF) was used for all major elements except for Re. Re contents were determined using inductive coupled plasma atomic emission spectroscopy (ICP-AES). These measurements were performed for the five reference segments A2, C1, C2, C3, and E2 of plate ERBO/1C-1/6. Details of the post cast heat treatment of our alloy are given in Table 2.

## 2.2. Optical Microscopy (OM), Scanning Electron Microscopy (SEM), Electron Probe Microanalysis (EPMA) and Scanning Transmission Electron Microscopy (STEM)

Good optical and SEM micrographs can be obtained from specimens, which were polished down to a mesh size of 1  $\mu\text{m}$  and then electropolished using a Struers A2 electrolyte (applied voltage: 5 V; time: 6–10 s; flow rate: 12). An OM and a SEM of type JEOL JSM-6490 were used to study the dendritic cast microstructure. The JEOL JSM-6490 was equipped with an orientation imaging electron back scatter diffraction (EBSD) system, which allows to measure crystallographic orientations, which can be presented using color coding. As shown in Figure 2a, the red color ( $\langle 001 \rangle$  direction) extends over almost the whole SX plate. The EBSD results prove that the specimen is a single crystal with only small regions with cast defects (such as tiny grains of different color in the red region of Figure 2a). The distribution of alloy elements in the cast microstructure (dendrite cores and ID regions) were investigated using an electron probe micro analyzer of type Cameca SX 50. TEM specimens were prepared using electrochemical thinning in a Struers TenuPol 5 (electrolyte: 75% methanol, 15% perchloric acid, 10% glycerol; applied voltage: 12 V; temperature:  $-15^\circ\text{C}$ ; flow rate: 35). In addition, thin foils were prepared using focused ion beam (FIB) milling in a FEI Quanta 300 3D. TEM investigations were performed using a Tecnai G<sup>2</sup> F20 from FEI, equipped with an EDX analysis system, operating at 200 kV in the scanning transmission (STEM) mode. STEM was used to obtain images of the  $\gamma/\gamma'$  microstructure. EDX measurements were performed in order to obtain a first impression of element partitioning between  $\gamma$  and  $\gamma'$ .

Table 2. Specification of post-cast heat treatment for ERBO/1C-1.

Solution treatment	RT ( $20^\circ\text{C min}^{-1}$ ) $\rightarrow$ $1290^\circ\text{C}$ for 1 h ( $1^\circ\text{C min}^{-1}$ ) $\rightarrow$ $1300^\circ\text{C}$ for 6 h ( $150^\circ\text{C min}^{-1}$ ) $\rightarrow$ $800^\circ\text{C}$ (air cooled) $\rightarrow$ RT
Precipitation treatment	$1140^\circ\text{C}$ for 4 h $\rightarrow$ $870^\circ\text{C}$ for 16 h $\rightarrow$ RT

### 2.3. Characterization of Elastic Properties and Creep Testing

Figure 2c schematically illustrates how specimens were obtained from plate segments. After casting, SX plates can show deviations of several degree from the ideal  $\langle 001 \rangle$  solidification direction. Precisely oriented specimens (deviation  $<1^\circ$ ) can be manufactured combining crystallographic alignment of plate segments using the Laue technique and subsequent electro-discharge machining. Such specimens are required to determine elastic constants and creep properties. In the case of the rectangular parallelepipeds required for the measurements of elastic constants, the geometric density  $\rho_G = M/(L_1 L_2 L_3)$  calculated from sample mass  $M$  and dimensions  $L_i$  agree well with  $\rho_B = 8.67(3) \text{ g cm}^{-3}$  obtained by the buoyancy method in pure water (see Table 5 in Section 3). Elastic constants at room temperature were derived from the resonance frequencies of freely vibrating rectangular parallelepipeds utilizing resonant ultrasound spectroscopy (RUS).<sup>[12]</sup> RUS allows determining all independent elastic constants of a single sample from its resonance spectrum with high consistency. Resonance spectra were collected between 150 and 800 kHz on rectangular parallelepipeds with edges parallel to the axes of the cubic reference system of the superalloy SX and edge lengths between 5 and 7.5 mm. For each specimen at least 50 eigenfrequencies were used to calculate the three independent elastic constants assuming cubic symmetry of the macroscopic specimen. Creep tests were performed on specimens with  $[001]$  orientation at 1323 K and 160 MPa using constant load creep machines, following a miniature creep specimen test procedure, which has been described in the literature.<sup>[13,14]</sup>

### 2.4. High Resolution Characterization Methods

To study the physical nature of  $\gamma/\gamma'$  interfaces on the atomic scale the complementary high-resolution techniques, HRTEM,<sup>[15,16]</sup> and APT were used.<sup>[17,18]</sup> In the framework of the present study, we do not give a full account of these two methods. Our objective is to provide a few examples of the type of information, which can be obtained using these methods, that can help to gain a better understanding of elementary processes during creep. For example, dislocations which form at  $\gamma/\gamma'$  interfaces in the early stages of creep govern the high temperature plasticity of single crystal superalloys.<sup>[19]</sup> HRTEM and APT can help to analyze the nature of such interface dislocations in detail, with emphasis being placed on strain fields around dislocations and on segregation phenomena at dislocation lines. High-resolution techniques are also important to study tiny microstructural features with sizes in the nanometer range. HRTEM samples were prepared by conventional mechanical thinning followed by  $\text{Ar}^+$  ion milling using a Gatan Precision Ion Polishing System (PIPS). For the  $\text{Ar}^+$  ion milling, a two-step process was established. In the first step, 3 keV ions were used which produce an electron transparent hole in sufficiently short time. In the second step, ion milling at 700 eV and  $-15^\circ\text{C}$  removes a thin amorphous layer. To investigate the core structure of an interface dislocation which formed during high temperature

$\langle 001 \rangle$  tensile creep, a specimen crept to a strain of 0.4% was investigated. The HRTEM images were taken using an aberration corrected FEI Titan<sup>3</sup> 80–300 microscope operating at an acceleration voltage of 200 kV. APT analyses were performed using a local electrode atom probe (LEAP<sup>TM</sup> 3000X HR, Cameca Instruments) in voltage mode at a specimen base temperature of  $\approx 65 \text{ K}$ . The pulse fraction and the pulse rate were 15% and 200 kHz, respectively. Data reconstruction and analysis was performed using the Cameca IVAS<sup>TM</sup> 3.6.6 software package. The first subset of  $\approx 1$  million collected ions was discarded from the analysis to exclude the zone damaged by  $\text{Ga}^+$  ions during FIB milling. Spatial and mass resolution provided by the LEAP was high enough for accurate and reliable characterization of the elemental distribution at a length scale of  $\leq 1 \text{ nm}$ . APT specimens were prepared using a dual-beam focused-ion-beam (FIB) system (FEI Helios Nanolab 600) by the conventional lift-out technique described in ref.<sup>[20]</sup> The features of the cast microstructure were considered prior to the lift-out procedure to allow target preparation of the specimens both from dendrite cores and ID areas. To minimize implantation of Ga ions, beam intensity was reduced to 5 keV for final shaping of the APT tips.

## 3. Results

### 3.1. Dendrites and Interdendritic Regions

The chemical differences between the D and ID regions result in the distinct contrast in the optical micrograph presented in Figure 3a. D and ID regions represent the large-scale microstructural heterogeneity (length scale:  $300 \mu\text{m}$ ), which characterizes all cast single crystal Ni-base superalloys. The optical micrograph presented in Figure 3a extends across the whole cross section of the SX plate, which was investigated in the present study.

Figure 3a shows that there are finer and more closely spaced dendrites in the outer regions of the plate, where cooling was faster. In order to assess the large-scale heterogeneity of the microstructure, an effort was made to determine parameters, which define the dendrite/interdendrite morphology of the plate ERBO/1C-1/6. We assess the homogeneity in the vertical direction of the plate, comparing the top (A2 in Figure 2b), middle (C2 in Figure 2b) and the bottom of the plate (E2 in Figure 2b). We also analyze whether there is heterogeneity in the cast microstructure in the horizontal direction, comparing the left, middle, and right part of plate ERBO/1C-1/6 (locations C1–C3 in Figure 2b). As Warnken and Reed<sup>[21]</sup> have discussed, it is not a simple task to define a meaningful procedure for measuring spacings between dendrite cores.

In the present study, we take a pragmatic approach and measure dendrite spacings from montages such as the one shown for location C3 (see Figure 2b), from the cast and heat treated plate ERBO/1C-1/6, Figure 3b. In Figure 3b, the dendrites can be clearly distinguished, even after a full homogenization heat treatment, where the chemical composition of the dendrites no longer reflects the chemical



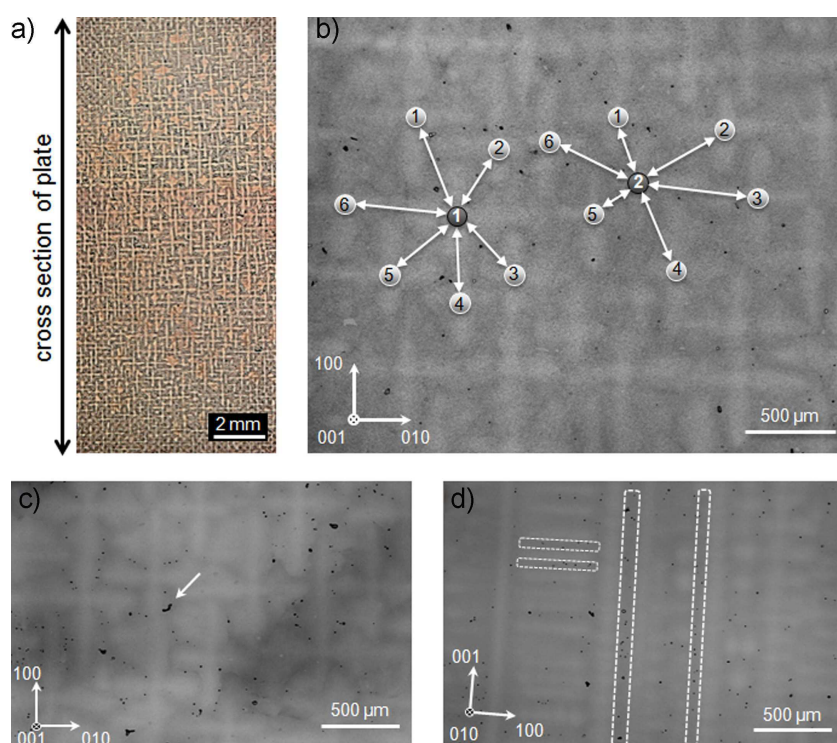


Fig. 3. Micrographs revealing defects of the cast microstructure. (a) Optical micrograph, which shows the full cross section of the plate. Dendrites and interdendritic regions can be clearly distinguished. (b) SEM back scatter electron micrograph with dendrites (light gray crosses) and interdendritic regions (dark gray regions). (c) Back scatter electron SEM micrograph of cast micropores in a cross section perpendicular to the solidification direction. (d) Back scatter electron SEM micrograph of cast micropores in a cross section parallel to the solidification direction.

condition directly after casting. In Figure 3b, the dendrites appear as light gray crosses separated by dark gray ID regions. The evaluated cross section has an area of  $6.2 \times 5.1 \text{ mm}^2$ . In the present study, we evaluate dendrite spacings by first selecting one central dendrite, marked with 1 in the SEM back scatter micrograph of Figure 3b. For this central dendrite, we measure the distances to its direct neighbors (1–1, 1–2, ..., 1–6). We then move on to a next dendrite, marked with a 2, which does not share direct neighbors with the first dendrite, and measure the distances 2–1, 2–2, ... 2–6. We repeat this procedure for other dendrites, which neither share direct neighbors with each other nor with dendrites 1 and 2. In the case of the cross section C3 shown in Figure 3b (specimen reference: ERBO1/C1/6-C3), there is a total number of 123 dendrites. From these, 16 central dendrites were selected and 95 individual dendrite spacings were measured. A simple mean value for the average spacing can be obtained by dividing the total area of the cross section  $31.62 \text{ mm}^2$  by the total number of dendrites. Interpreting the resulting mean area per dendrite as a square, the length of one side of the square represents an average dendrite spacing (result for C3:  $505 \mu\text{m}$ ). In the following, we consider the distribution of 95 individual dendrite spacings, which were measured for plate segment C3.

The resulting histogram is shown in Figure 4a. Figure 4a shows that the measurements for the plate segment C3 have a

distinct maximum close to  $500 \mu\text{m}$ , as one would expect from our simple mean value estimate. Figure 4a also reveals that dendrite spacings show high scatter. For plate segment C3, we find dendrite spacings ranging from 250 to  $762 \mu\text{m}$ . Figure 4b shows the distribution of dendrite spacings from all plate locations considered (A2, C1–C3, and E2). Presenting all dendrite spacing measurements in one histogram does increase the width of the distribution but does not alter the position of the maximum of the distribution. We now present the dendrite spacing results obtained for the different plate locations, Figure 4c–d. Figure 4c and d shows how average dendrite spacings evolve in the vertical direction of the plate. In Figure 4c, we plot the mean value of all individual dendrite spacing measurements for the top A2, middle C2, and bottom E2 segments in Figure 2b. In Figure 4d, we present the average area per dendrite, which was obtained by dividing the area of the evaluated cross section by the total number of dendrites for the top, middle, and bottom position of the plate. In Figure 4e, we show how the mean value of the individual spacings changes across the plate, plotting the data for the left C2, middle C3, and right side C4 of the plate (see Figure 2b). Figure 4f shows how the average area per dendrite

changes across the plate. In the light of the large width of individual dendrite spacing distributions, the results presented in Figure 4 show that there is no big difference between dendrite spacings measured at different plate locations. However, the results also show that dendrite spacings decrease from the top A2 to the bottom of the plate E2. They also suggest that dendrite spacings decrease as we cross the plate from the left C1 to the right C3.

Figure 3c and d shows SEM micrographs, which document the presence of micro porosity in the plate ERBO1/C1/6, after casting followed by a post cast heat treatment. In Figure 3c, a white arrow highlights one large pore in an ID region. Figure 3c was taken from a cross section perpendicular to the solidification direction. A clear correlation between the locations of dendrites and pores is not obvious. However, in the SEM micrograph taken from a cross section parallel to the solidification direction, one can see that pores line up along primary dendrites, Figure 3d. Pores form between secondary dendrite arms close to the primary dendrite branches, as has been reported by Mälzer *et al.*<sup>[13]</sup>

### 3.2. Average Alloy Composition and Partitioning of Elements in the Cast Microstructure

Six sets of chemical results were obtained for the concentrations of elements in our alloy by means of XRF (all major alloy elements except Re) and ICP-AES (Re). The

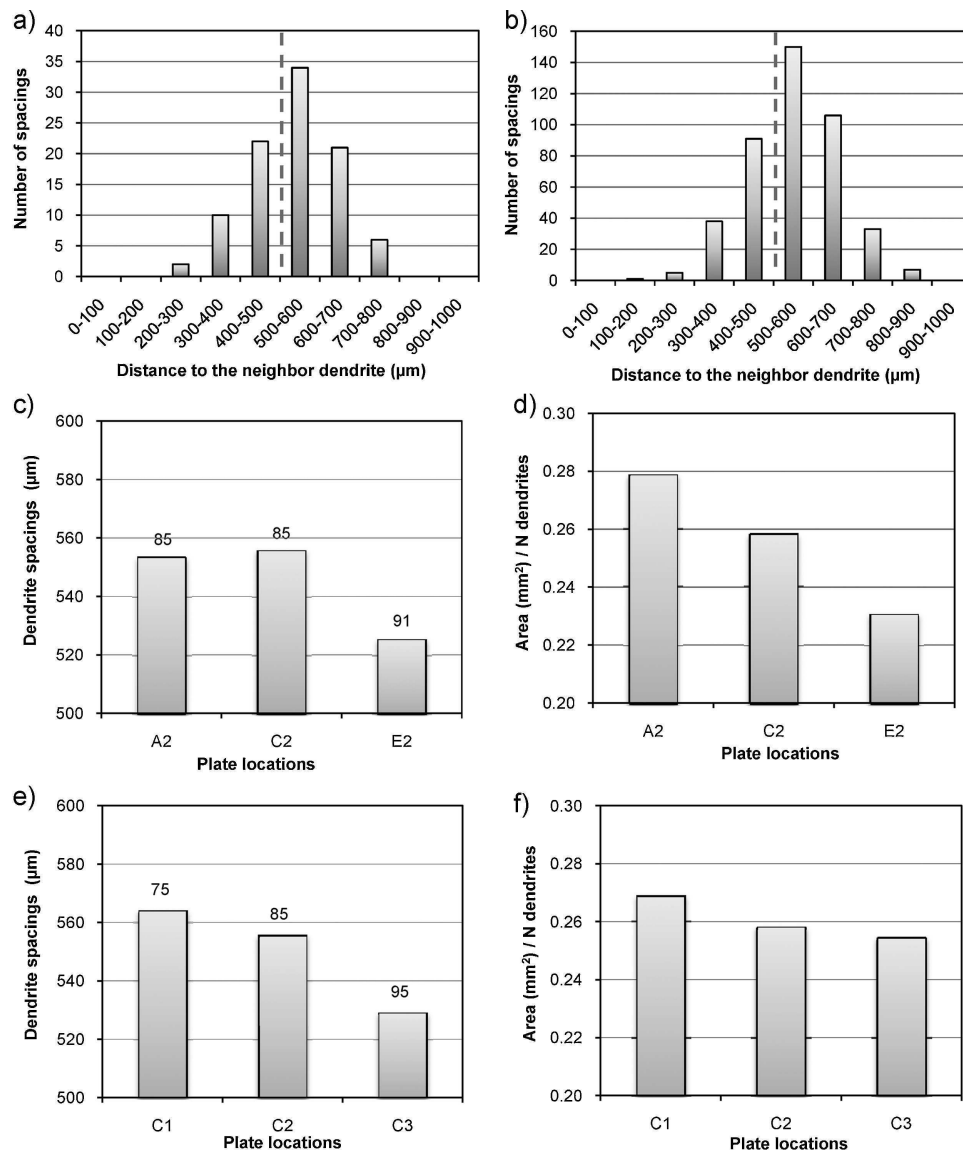


Fig. 4. Histograms showing the distribution of dendrite spacings is included as a dashed vertical line. (a) Local results for cross section of plate segment C3. (b) Results from all plate locations (A2, C1–C3, and E2). Dendrite spacings for different plate locations (see Figure 2b). (c) Evolution of mean value along the vertical plate direction (A2 → C2 → E2). (d) Evolution of average area per dendrite in the vertical plate direction (A2 → C2 → E2). (e) Evolution of mean value along the horizontal plate direction (C1 → C2 → C3). (f) Evolution of average area per dendrite along the horizontal plate direction (C1 → C2 → C3).

results are presented in Table 3. One material state (first column in Table 3) was investigated in the as cast condition (ERBO/1A). The other measurements were performed for the five plate segments A2, C1, C2, C3, and E2 shown in Figure 2b (heat treated conditions, ERBO/1C). The results presented in Table 3 clearly show that the post cast heat treatment does not affect the alloy composition. The results also show that the plate investigated in the present study has a good chemical homogeneity on the macro-scale.

In the following, we provide experimental evidence, which shows that alloy elements are not homogeneously distributed in the microstructure of our single crystal Ni-base superalloy. We first consider the distribution of alloy elements in D and ID regions. Figure 5 shows four color-coded WDX-EPMA maps,

which document the distribution of the elements Al and Re in the microstructure. Figures 5a and b shows distribution of Al in the as cast condition and after heat treatment, respectively. In Figure 5c and d, we present Re distributions before and after heat treatment, respectively. The color coding on the right side of the element distribution maps does not specifically account for actual concentrations. Instead it simply qualitatively interprets the number of counts in terms of normalized maximum (value: 1) and minimum (value: 0) concentrations. Figure 5a and c shows that during solidification segregation processes result in an enhanced Al concentration in the ID regions, while Re partitions to the dendrites. As can be seen from Figure 5b and d, the post cast heat treatments, results in a more homogeneous distribution of

Table 3. Concentration of major alloy elements obtained from two material states.

Local average compositions [wt%]										
Elements	Al	Co	Cr	Hf	Mo	Re	Ta	Ti	W	Ni
ERBO/1A-1/9-A2	5.8	9.3	6.2	0.1	0.6	2.9	6.9	1.0	6.3	Bal.
ERBO/1C-1/6-A2	5.7	9.4	6.2	0.1	0.6	2.9	6.7	1.0	6.7	Bal.
ERBO/1C-1/6-C1	5.7	9.5	6.3	0.1	0.6	2.8	6.7	0.9	6.6	Bal.
ERBO/1C-1/6-C2	5.6	9.4	6.3	0.1	0.6	2.8	6.7	0.9	7.0	Bal.
ERBO/1C-1/6-C3	5.7	9.3	6.1	0.1	0.6	2.9	6.8	1.0	6.3	Bal.
ERBO/1C-1/6-E2	5.8	9.3	6.1	0.1	0.6	2.8	6.8	1.0	6.3	Bal.

One material state represents the as cast condition of alloy ERBO/1A-1/9. The other five sets (A2, C1–C3, and E2) of results were obtained from different locations of the plate shown in Figure 2b after heat treatment (ERBO/1C-1/6).

both elements. But even after the homogenization treatment, there is more Al in the ID regions than in the dendrites, Figure 5b, and more Re in the dendrites, Figure 5d. Figure 5a and c shows the same microstructural region. It can be clearly seen that there is less Al in the dendrites (blue) than in the surrounding regions (green/yellow), Figure 5a. In contrast, there is more Re in the dendrite (yellow/red) than in the ID regions, Figure 5c. The strong partitioning, which leads to the element distributions shown in the element distribution maps of Figure 5a and c is counteracted by the heat treatment. As can be seen in Figure 5b and d, the element distributions become more homogeneous but different levels of concentrations can still be distinguished, especially for Re in Figure 5d.

In Table 4, we present quantitative chemical results, which were obtained from EMPA point analyses and appropriate data treatments for all major alloy elements in a fully heat-treated material from the five reference segments highlighted in blue in Figure 2b. For this analysis, the electron beam was focused onto the center of a dendrite and in the middle of an ID region, respectively. Table 4 is subdivided into three sections. In the upper part of Table 4, we present concentrations, which were measured in the dendrite core. The results from the ID regions are presented in the middle part of Table 4. And at the bottom of Table 4 we show partitioning coefficients  $k'$ , which represents the ratio of the concentrations measured in the D and the ID regions:

$$k' = \frac{c_D}{c_{ID}} \quad (1)$$

All elements with  $k' < 1$  partition to the ID regions. The elements with  $k' > 1$  are enriched in the dendrite cores. When  $k = 1$  there is no preference of the corresponding alloy element with respect to specific locations in the microstructure. Comparing Table 3 and 4, we find that there is good agreement between the average XRF data and the local EPMA data. In fact, as one would expect, the average XRF results yield values, which fall right in between the EPMA data, which were obtained for D and ID regions (e.g., for Al and Re).

For elements which do not partition,  $k' \approx 1$  (e.g., for Co and Cr), the two methods yield the same results.

### 3.3. STEM and EDX Analysis in the TEM

The STEM micrograph in Figure 6a was obtained using a high angle annular dark field (HAADF) detector in an analytical TEM. We note that there are tiny spherical particles within the  $\gamma'$  cubes and we will show later that these particles represent spheroidal  $\gamma$  phase particles, which homogeneously precipitate from the  $\gamma'$  matrix during cooling from the high temperature regime.

Figure 6b shows a conventional high-resolution TEM image of a round dark particle in a light gray matrix. Individual atom columns can be distinguished. In Figure 6c, we present results obtained using a fast Fourier transformation (FFT) algorithm, which is part of the Digital Micrograph software package from Gatan and which translates real space periodicity into reciprocal space. As a result, for the matrix we obtain intensities, which represent a cut through the reciprocal lattice of the ordered  $L1_2$  phase, Figure 6c. As one would expect, Figure 6c shows extra spots, which indicate the  $L1_2$  order. In contrast, the FFT analysis of the particle in Figure 6d shows no extra spots and this allows to conclude that it has an fcc crystal lattice. We now show element concentrations obtained with the analytical TEM for the  $\gamma$  channels and the  $\gamma'$  cubes (small scale heterogeneity of our material). The chemical compositions were obtained using energy dispersive X-ray spectroscopy in the Tecnai G<sup>2</sup> F20 TEM. The results were obtained from a TEM foil, which was taken from section A3 of the investigated plate ERBO/1C-1/6.

Two series of EDX maps covering the elements Al, Co, Cr, Ni, Re, Ta, Ti, and W are presented in Figure 7a and b. The upper series of EDX maps were recorded in ID regions, Figure 7a. The lower series of EDX maps was measured close to a dendrite core, Figure 7b. The color for each element has been arbitrarily chosen and a brighter intensity indicates a higher concentration. The results presented in Figure 7a and b are qualitative, not quantitative. Thus, for example, in the upper left of Figure 7a, the red color shows the presence of more Al in the  $\gamma'$  phase while the dark contrast indicates that there is less Al in the  $\gamma$  channels. Figure 7a and b shows that



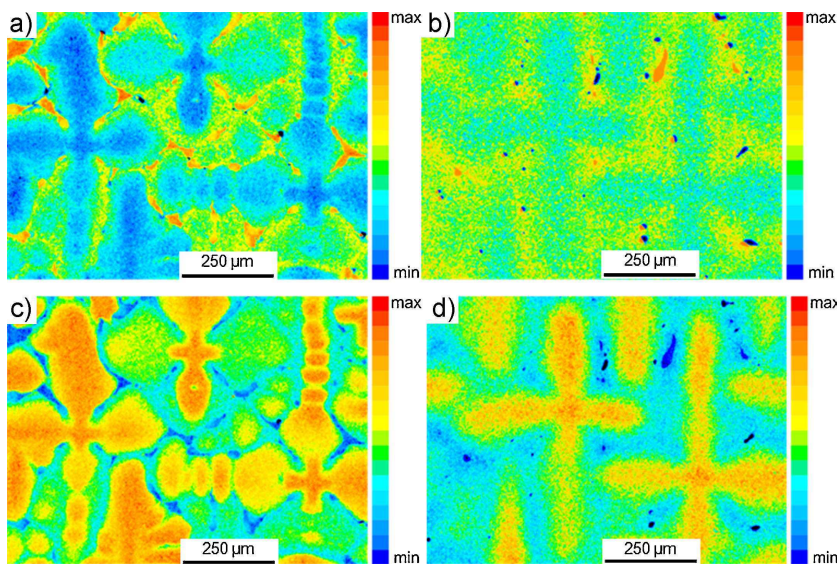


Fig. 5. Element mapping of Al and Re performed using EPMA. (a and c) As cast conditions. (b and d): Heat-treated conditions. (a) Al distribution in as cast condition. (b) Al distribution after heat treatment. (c) Re distribution in as cast condition. (d) Redistribution after heat treatment.

the elements Al, Ni, Ta, and Ti have a tendency to partition to the  $\gamma'$  cubes while the elements Co, Cr, Re, and W show higher concentrations in the  $\gamma$  channels. Figure 7a and b also shows that these trends do not depend on whether we investigate ID (upper rows of Figure 7a and b) or dendritic (lower rows in Figure 7a and b) parts of the microstructure.

The results from EDX point analyses are presented in Figure 8a and b. Figure 8a shows results, which were obtained from a region close to a dendrite core, while the results

presented in Figure 8b were measured in the center of an ID region. The four columns for each element represent different concentrations. The first column represents a concentration in the  $\gamma$  channel (orange). The second column shows the concentration of a  $\gamma'$  particle. The third column (green) represents an average concentration, which was calculated based on a weighted mean value, which was obtained by simply assuming that our alloy has a  $\gamma'$  volume fraction of 0.7:

$$\bar{c} = 0.3c_{\gamma} + 0.7c_{\gamma'} \quad (2)$$

The fourth column (black) represents the as specified composition of the alloy (Table 1), for comparison.

### 3.4. Mechanical Properties

The elastic constants of the samples taken from the heat-treated ERBO/1C plate show only small variations of less than 1%, indicating on the one hand the good large scale elastic homogeneity of the plate and on the other hand the high efficiency of the RUS method, Table 5. The scattering of the  $c_{ij}$  is significantly larger for the samples taken from the as cast state (ERBO/1A), which is probably a consequence of the more pronounced chemical inhomogeneities between dendrites and ID regions. However, the elastic stiffnesses of all our samples are well within the range of data reported for CMSX-4 in the literature, Table 5.

Table 4. Quantitative results on concentrations obtained by WDX-EPMA point analysis from dendrite cores and interdendritic regions after heat treatment in the five reference segments A2, C1–C3, and E2.

Element	Al	Co	Cr	Hf	Mo	Re	Ta	Ti	W	Ni
Dendrite core (wt%)										
ERBO/1C-1/6-A2	5.6	9.9	6.7	0.1	0.6	4.0	5.6	1.0	8.4	bal.
ERBO/1C-1/6-C1	5.7	9.8	6.9	0.1	0.6	4.0	5.5	0.9	7.9	bal.
ERBO/1C-1/6-C2	5.6	9.3	6.2	0.1	0.6	3.5	5.7	1.0	8.1	bal.
ERBO/1C-1/6-C3	5.7	9.7	6.5	0.0	0.5	3.9	5.8	0.9	7.7	bal.
ERBO/1C-1/6-E2	5.9	9.5	6.1	0.1	0.6	3.6	6.1	1.0	7.5	bal.
Interdendritic region (wt%)										
ERBO/1C-1/6-A2	6.3	9.3	6.0	0.1	0.5	1.9	7.1	1.1	5.3	bal.
ERBO/1C-1/6-C1	6.1	9.7	6.7	0.1	0.6	2.3	6.5	1.0	5.7	bal.
ERBO/1C-1/6-C2	6.2	9.4	6.2	0.1	0.6	2.2	6.7	1.1	5.7	bal.
ERBO/1C-1/6-C3	6.2	9.5	6.4	0.1	0.6	2.3	6.8	1.1	5.6	bal.
ERBO/1C-1/6-E2	6.4	9.1	5.9	0.1	0.6	1.8	7.1	1.1	5.8	bal.
Partitioning coefficient										
$k'_{A2}$	0.9	1.1	1.1	0.5	1.1	2.1	0.8	0.9	1.6	0.9
$k'_{C1}$	0.9	1.0	1.0	0.6	1.1	1.7	0.8	0.9	1.4	1.0
$k'_{C2}$	0.9	1.0	1.0	0.6	1.1	1.6	0.8	0.9	1.4	1.0
$k'_{C3}$	0.9	1.0	1.0	0.6	0.9	1.7	0.8	0.9	1.4	1.0
$k'_{E2}$	0.9	1.0	1.0	1.0	0.9	2.0	0.9	0.9	1.3	1.0

Upper part: results from dendrite cores. Middle: results from interdendritic regions. Lower part: corresponding partitioning coefficients.



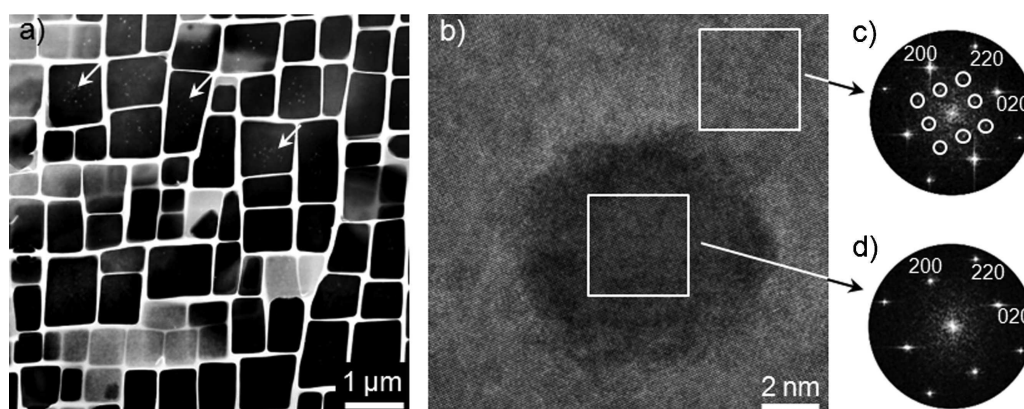


Fig. 6. Scanning transmission electron microscopy (obtained using a high angle annular dark field, HAADF, detector). (a) Cuboidal  $\gamma'$  particles (dark) are separated by thin  $\gamma$  channels (bright). Tiny spherical bright spots (a few highlighted with white arrows) within the cuboidal  $\gamma'$  particles represent  $\gamma$  phase particles. (b) High-resolution TEM micrograph of a spherical  $\gamma$  particle in the  $\gamma'$  phase. (c) Fast Fourier transform of ordered matrix. Extra spots highlighted with white circles. (d) Fast Fourier transform of fcc precipitate.

Figure 9 shows creep curves, which were obtained from miniature creep specimens from the five reference locations A2, C1–C3, and E2 shown in Figure 2b. The experiments were taken through to rupture. As can be seen from Figure 9a, the five creep curves almost coincide up to 100 h. There is a small scatter in rupture times ( $\Delta t_R = 40$  h) and in rupture strain ( $\Delta \epsilon_R = 12\%$ ). Figure 9b shows that all five creep experiments yield the same minimum creep rate of  $4 \times 10^{-8} \text{ s}^{-1}$ .

### 3.5. High Resolution TEM and Atom Probe Tomography

So far we have presented results, which were obtained with conventional methods. We have seen that our laboratory plate features the type of large and small-scale heterogeneities, which we expect for single crystal superalloys. We now show some examples, which illustrate what further information can be obtained using high-resolution methods. The results shown in Figure 10 were obtained using a FEI Titan<sup>3</sup> 80–300 HRTEM. Figure 10a shows an FFT filtered micrograph of the  $\gamma/\gamma'$  transition region. A horizontal rectangle (width: approximately 4 unit cells, length: approximately 14 unit cells) extends from the  $\gamma$  phase on the left to the  $\gamma'$  phase on the right of the image. No sharp interface can be identified. An intensity profile was measured along the long axis of the reference rectangle. The intensity results were averaged over the 4 unit cells. The resulting intensity profile is plotted in Figure 10b. Figure 10b indicates that constant peak intensities are observed in the cubic face centered  $\gamma$  phase with a statistical distribution of atoms over the lattice sites (no chemical ordering; left side of Figure 10b). In contrast, the lattice site occupancy in the ordered  $L_{12}$  crystal lattice of the  $\gamma'$  phase results in oscillating peak intensities (right side of Figure 10b). Most importantly no sharp interface is observed between the  $\gamma$  and the  $\gamma'$  phase. Instead, we observe a 1.4 nm transition region, which extends over four unit cells (from position  $x_1$  to position  $x_2$  in Figure 10b). The results presented in Figure 10b show that the long range ordering gradually disappears over 4 unit cells, as we move from the  $\gamma'$  phase on the right to the  $\gamma$  phase on the left of Figure 10a and 10b. After 0.4% creep deformation, the  $\gamma/\gamma'$  interface is

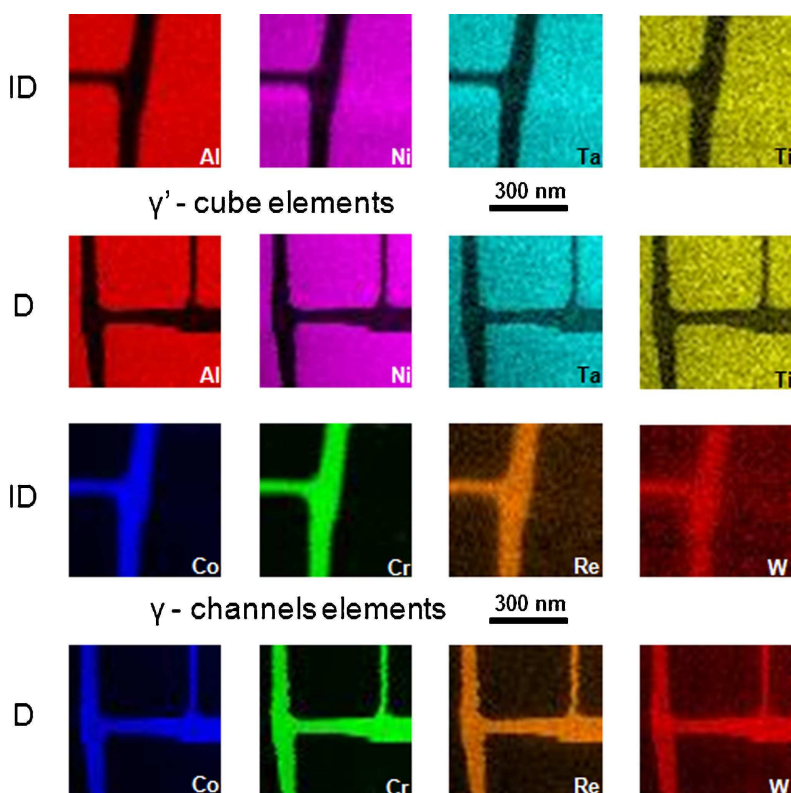


Fig. 7. Series of EDX maps obtained using TEM, showing the partitioning of Al, Co, Cr, Ni, Re, Ta, Ti, and W in our single crystal superalloy. (a) Alloy elements, which partition to  $\gamma'$  (upper row – interdendritic region, lower row – dendrite core). (b) Alloy elements, which partition to  $\gamma$  (upper row – interdendritic region, lower row – dendrite core).

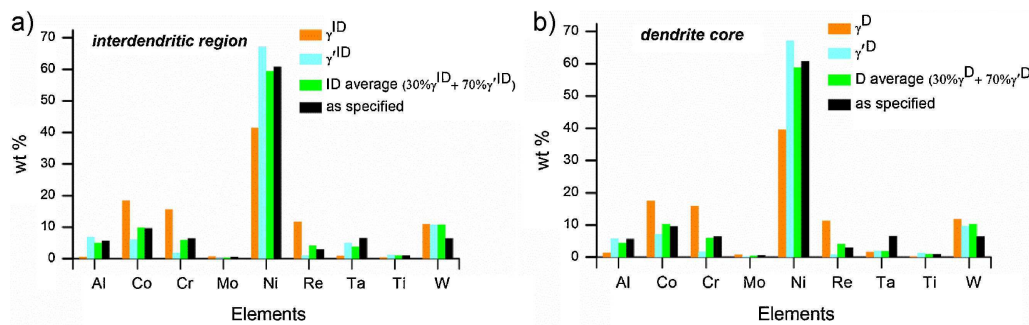


Fig. 8. Experimental (EDX, TEM: Tecnai G<sup>2</sup> F20), calculated and specified chemical compositions. Compositions of  $\gamma$  channels and  $\gamma'$  cubes and average alloy compositions for major alloy elements. The four columns for each data set represent concentrations of a  $\gamma$  channel (orange), of a  $\gamma'$  particle, the average concentration in the dendrite core calculated based on Equation (2) (green) and the nominal chemical composition of the alloy (black). (a) Interdendritic regions. (b) Dendrite cores.

even less well defined. This is partly related to the directional coarsening of the  $\gamma'$  particles, where  $\gamma'$  cubes change into elongated  $\gamma'$  rafts. It is also related to the accumulation of interface dislocations at the  $\gamma/\gamma'$  interfaces during creep. Figure 10c shows a curved  $\gamma/\gamma'$  interface (position marked with a green dashed line) of a sample with  $[-110]$  zone axis orientation. The region highlighted by a red square in Figure 10c is shown at a higher magnification in Figure 10d. Figure 10d shows an interface dislocation, which has formed during creep. The dislocation in Figure 10d is in a region where the  $\gamma/\gamma'$  interface is curved. By performing a Burgers circuit analysis, the dislocation in Figure 10d was identified as a  $60^\circ$  mixed dislocation gliding on a  $(111)$  plane with a Burgers vector of  $a_0/2 [0-11]$ .

In this configuration, the associated additional half plane points toward the  $\gamma'$  phase and therefore accommodates the elastic strain energy associated with the negative misfit between both phases (the  $L1_2$  lattice constant of the  $\gamma'$  phase is smaller than the fcc lattice constant of the  $\gamma$  phase). The dislocation shown in Figure 10d represents just one type of interface dislocation, which forms during creep, other interface dislocations are present, which are not addressed in the present study. Here, it is important to highlight that HR

TEM allows studying details of end on oriented linear lattice defects at  $\gamma/\gamma'$  interfaces.

We now present the results obtained by APT, which is a 3D method for elemental analysis with a spatial resolution of  $\leq 1$  nm. This enables an accurate characterization of the concentrations of alloy elements in the thin  $\gamma$  channels of Ni-base superalloys. An APT element map of ERBO/1C-1 showing the distributions of Al, Cr, and Re, is shown in Figure 11a. The  $\gamma$  phase on the top of Figure 11a appears green and orange because it is rich in Cr (color coding: green) and Re (color coding: orange). The  $\gamma'$  phase in the lower part of the image appears blue, due to its high content in Al (color coding: blue). At the right hand side of the figure, the corner of a  $\gamma'$  precipitate is approached and the  $\gamma/\gamma'$  interface curves down. APT measurements show that Al, Ta, Ti, and Hf partition to the  $\gamma'$  precipitates. All other major alloy elements predominantly reside in the  $\gamma$  matrix.

In Figure 11b, we present the corresponding concentration profiles of Cr, Al, and Re and in addition the concentration profiles of Co and Ta across the  $\gamma/\gamma'$  interface. The concentration data are presented as proximity histograms following the procedure of Hellman *et al.*<sup>[25]</sup> Figure 11b shows that there is no elemental segregation at the interface. There

Table 5. Elastic constants of Ni-base superalloys at room temperature.  $c_{ij}$  are elastic constants in GPa,  $\rho_G = M/(l_1 l_2 l_3)$  denotes the geometric density calculated from sample mass  $M$  and dimensions  $l_i$  in  $\text{g cm}^{-3}$ .

Material	ERBO/1A-1/ 8-A6-1	ERBO/1A-1/ 8-A6-2	ERBO/1C-1/ 6-A3-1	ERBO/1C-1/ 6-A3-2	ERBO/1C-1/ 6-C1-7	CMSX-4	CMSX-4	Ni <sub>3</sub> Al
Condition	As cast			Heat treated				
Reference	Present work					[22]	[23]	[24]
$c_{11}$	254.7(1)	249.3(1)	247.8(1)	248.4(1)	247.7(1)	262	243	225
$c_{12}$	163.8(1)	157.8(1)	156.7(1)	157.1(1)	155.9(1)	161	153	149
$c_{44}$	131.4(2)	131.4(2)	131.2(2)	131.3(2)	130.0(2)	144	128	124
$\rho_G$	8.69(1)	8.71(1)	8.70(1)	8.69(1)	8.70(1)	—	—	—

Numbers in parentheses indicate the standard deviation of the last digit as derived from the covariance matrix of the fully converged least-squares refinement. Data for CMSX-4 and for Ni<sub>3</sub>Al from ref.<sup>[22–24]</sup>

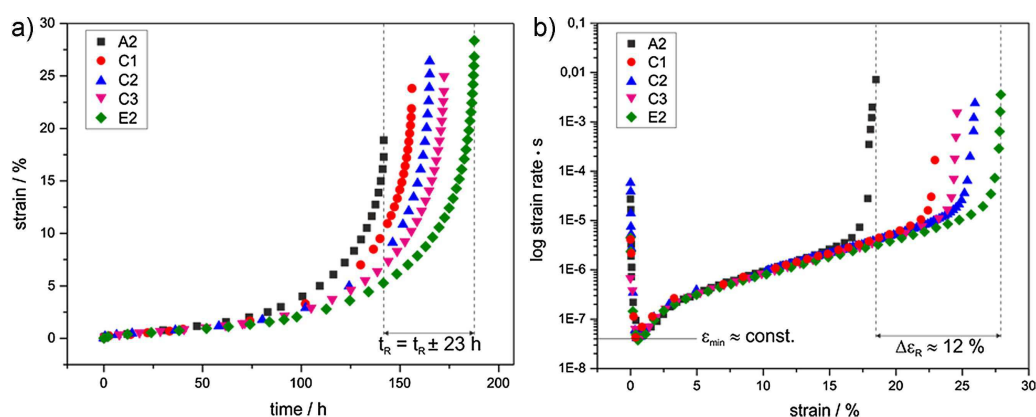


Fig. 9. Miniature specimen creep data from five reference locations A2, C1–C3, and E2 from Figure 2b. Stress and temperature: 160 MPa and 1323 K, respectively. (a) Strain versus time. (b) Strain rate versus strain in a log-linear plot.

are only slight pileups of Co, Cr, and Re in the  $\gamma$  phase close to the  $\gamma/\gamma'$  interface. This is probably related to the fact that as the  $\gamma'$  cubes grow, they push these elements into the  $\gamma$  matrix.

The elemental compositions obtained with APT independently for D or ID regions are summarized in Table 6. It clearly shows that only minor difference exists between the compositions of the  $\gamma'$  and  $\gamma$  phase in both regions. We therefore can make an attempt to use our Table 6 data in combination with the average chemical compositions from Table 4 (EPMA data) to obtain an estimate for the  $\gamma'$  phase

volume fractions in D and ID regions. We use a similar approach as in Equation 2 (mass balance equation reflecting the lever rule), but now we calculate volume fractions based on our measurements of chemical compositions:

$$\bar{c}_D = f_{\gamma'}^D c_{\gamma'}^D + f_{\gamma}^D c_{\gamma}^D = (1 - f_{\gamma'}^D) c_{\gamma'}^D + f_{\gamma'}^D c_{\gamma}^D \quad (3)$$

$\bar{c}_D$  represents the average concentration in dendrites as given in Table 4 (EPMA data).  $f_{\gamma'}^D$  and  $f_{\gamma}^D$  represents the volume fractions of the  $\gamma$  and  $\gamma'$  phases in the dendrites, respectively.  $c_{\gamma}^D$  and  $c_{\gamma'}^D$  represent the elemental compositions in D parts of the microstructure as measured using APT, Table 6. The equation was also applied correspondingly to the ID region. We can use our local chemical results in combination with Equation 3 to calculate  $\gamma$  and  $\gamma'$  volume fractions. We then obtain  $\gamma'$  volume fractions of  $72 \pm 1\%$  for dendrite cores and  $77 \pm 1\%$  for ID regions. In Figure 11c, we show two small spheroidal clusters depicted by 56 at% iso-concentration surfaces, which are enriched in Cr, Co, and Re (color coding: orange) and lean in Al (color coding: blue). The elemental concentrations inside the small particles are close to the composition of the  $\gamma$  matrix. This is in agreement with the TEM results presented in Figure 6 and confirms that tiny spherical  $\gamma$  particles form in the  $\gamma'$  precipitates. Figure 11d shows the microstructure of a crept specimen, which was interrupted after 1% strain. There are two features, which are not observed in the as heat-treated material, prior to creep. First, a small  $\gamma$  groove with a concave radius of about 5 nm has formed in the surface region of a  $\gamma'$  precipitate. The presence of this groove does not affect the concentrations of the adjacent  $\gamma'$  and  $\gamma$  phase regions. Second, inside the  $\gamma$  region on the right side of Figure 11d, numerous clusters with compositions similar to that of the  $\gamma'$  phase have appeared. Such  $\gamma'$  clusters

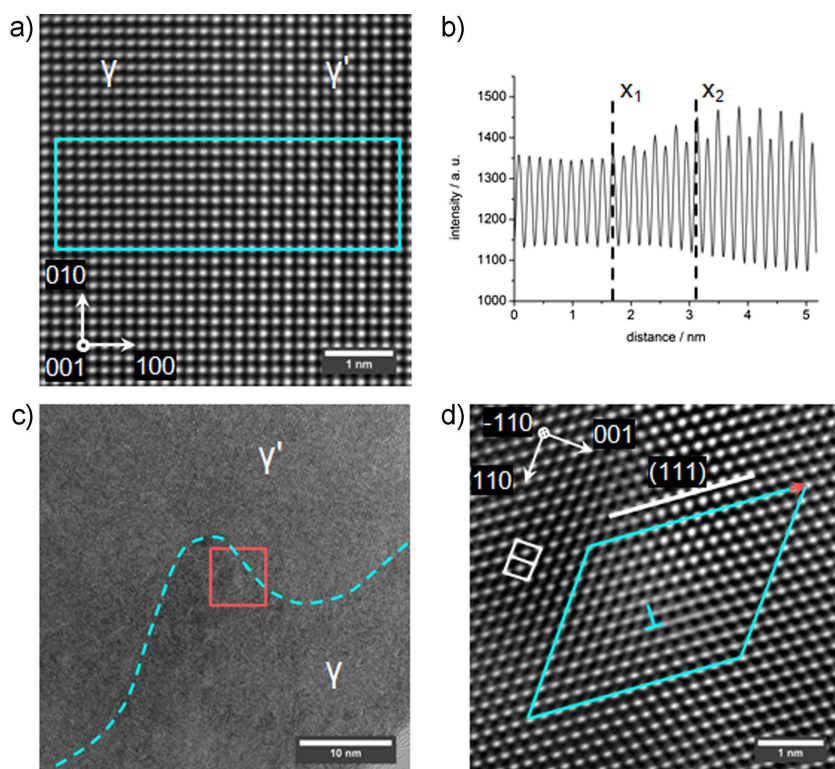


Fig. 10. Microstructural results obtained using HRTEM (FEI Titan<sup>3</sup> 80–300). (a) Fast Fourier transform (FFT) filtered image of a  $y/y'$ -interface prior to creep. (b) Corresponding intensity line profile across the interface. (c) Curved 0.4%  $y/y'$  interface after tensile creep. For details see text. (d) HRTEM image showing an extra half plane associated with a  $60^\circ$  interface dislocation.



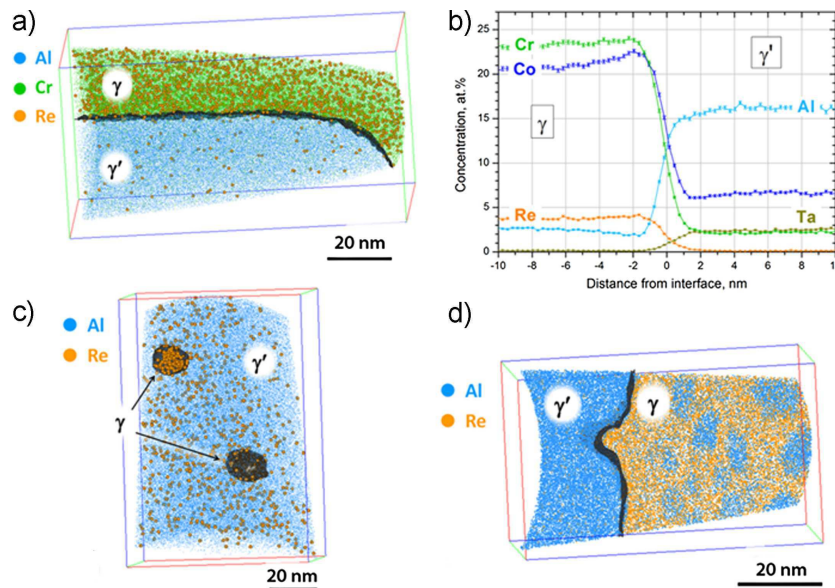


Fig. 11. Examples for results obtained using APT. (a) Elemental map of heat-treated alloy.  $\gamma$  (green/orange – color coding of Cr/Re) and  $\gamma'$  (blue – color coding of Al) regions are separated by a dark 58 at% Ni isoconcentration surface. (b) Concentration profiles of selected elements across the  $\gamma/\gamma'$  interface. (c) Distribution of elements in the interior of a large  $\gamma'$  precipitates documenting the presence of two tiny  $\gamma$  clusters (dark/orange). (d) Elemental map after creep at 1323 K and 160 MPa to 1% strain. There is a small groove in the  $\gamma/\gamma'$  interface with a concave radius of 5 nm. Numerous small  $\gamma'$  clusters (blue) have formed in the  $\gamma$  phase.

were not observed, at least in such a great number, in the heat-treated state prior to creep.

#### 4. Discussion

##### 4.1. Chemical Composition of Dendrites and Interdendritic Regions, Macroscopic Homogeneity

In the present study we use conventional and advanced characterization methods to do characterize two plates of the single crystal super alloy ERBO1, one in the as cast condition (reference: ERBO/1A-1/9) and another after heat treatment (reference: ERBO/1C-1/6). We show that the material features two microstructural heterogeneities. The solidification process results in a microstructure, which is characterized by dendrites and interdendritic regions. We refer to this large-scale heterogeneity as cast microstructure. The cast microstructure was quantified and an effort was made to

characterize the distribution of individual dendrite spacings  $d_D$  as well as to determine appropriate mean values. Our dendrite spacing measurements presented in Figure 4 suggest that different regions of the plates did not solidify at the same rate, there are small but significant differences in dendrite spacings measured at different plate locations. In agreement with what has been reported in the literature,<sup>[3,5,13,21]</sup> we find average dendrite spacings between 100 and 900  $\mu\text{m}$ , Figure 4. It is easy to detect the D/ID microstructure even after a full heat treatment, Figure 3. Segregation results in higher Re concentrations in the dendrite cores as compared to the interdendritic regions, Figure 5 and Table 4. The multiple step heat treatment outlined in Figure 1 and Table 2 results in a more homogeneous distribution of elements. But there is still more Re and less Al in the dendrites than in the ID regions, Figure 5 and Table 4. When material volumes are analyzed, with a size  $d_{\text{vol}}$ , which is significantly larger than the

Table 6. Compositions of  $\gamma$  matrix and  $\gamma'$  precipitates obtained from APT analysis.

Element	Al	Co	Cr	Hf	Mo	Re	Ta	Ti	W	Ni
$\gamma$ matrix (wt%)										
D	1.0	17.8	17.1	0	1.2	12.7	0.3	0.1	10.1	bal.
ID	1.2	17.9	17.3	0	1.3	11.8	0.4	0.1	9.4	bal.
$\gamma'$ precipitates (wt%)										
D	7.5	5.9	1.7	0.1	0.4	0.7	10.0	1.3	6.1	bal.
ID	7.6	6.0	1.8	0.1	0.4	0.5	9.7	1.4	5.5	bal.

Dendrite cores and interdendritic regions were analyzed independently.



characteristic size of our larger scale microstructural heterogeneity  $d_{lmh}$  (i.e.,  $d_{vol} \gg d_{lmh}$ ), our cast plate shows good homogeneity. This holds for average chemical compositions, Table 3. The chemical composition of our ERBO/1 alloys is very close to the specified composition, Table 1. And most importantly, this also applies to the elastic constants listed in Table 5 and to the creep properties at different locations from our plate, Figure 9. Figure 9 shows that precisely oriented creep specimens taken from different plate locations yield almost identical creep curves with very similar minimum creep rates. The creep behavior of different plate locations only differs with respect to rupture strains and rupture times. This is related to the heterogeneous distribution of cast pores in the microstructure, Figure 3c and d, as has been discussed by Mälzer *et al.*<sup>[13]</sup>

#### 4.2. Crystallographic and Chemical Width of the $\gamma/\gamma'$ Interface

According to our HRTEM analysis (Figure 10a and b) the order–disorder transition at the  $\gamma/\gamma'$  interface occurs over roughly 1.4 nm corresponding to 4 unit cells. This is slightly larger but close to the values obtained by Srinivasan *et al.*<sup>[26]</sup> for a Rene' 88 DT superalloy using HR STEM (1–1.3 nm) and APT (0.7–1 nm). We note here that TEM-based methods only provide an upper limit for the interface width since the inherent projection effect can lead to interface broadening (in case of an inclined or rough interface). Concerning the chemical transition there is controversy in the literature. Srinivasan *et al.*<sup>[26]</sup> report a huge width of the chemical transition, roughly twice as large as the order–disorder transition, based on HRSTEM ( $\approx 2.7$  nm) and APT ( $\approx 2.4$  nm) measurements. In contrast to these results, earlier work suggests<sup>[27,28]</sup> that there is a sharp chemical transition within only one atomic layer using 1D atom probe field-ion microscopy. A similar analysis of our APT data yields an interface width of maximum 0.5 nm. Although a much higher value can be derived from the proxigrams presented in the Figure 11c, the proxigrams are very sensitive to reconstruction and field evaporation artifacts in APT, and it appears to be a general problem in superalloy analysis. Further work is required to clarify this point.

#### 4.3. Dislocations and Grooves at $\gamma/\gamma'$ Interfaces

Interface dislocations have been reported to be associated with non-planar  $\gamma/\gamma'$  interfaces.<sup>[29,30]</sup> Kolbe *et al.*,<sup>[29]</sup> who first observed such interface irregularities, rationalized this observation with thermodynamic and kinetic arguments. From a thermodynamic point of view, the stress field of an interface dislocation can affect the local chemical potential of atoms and alter the driving force for diffusion. Interface dislocations can also provide pipe diffusion paths, which allow for fast transport of atoms from a horizontal  $\gamma'$  cube interface to a vertical one. If this would be the case, we expect to see an enrichment of diffusing atoms at the interface dislocation segment. Our HRTEM data (Figure 10c and d) clearly show that the groove at the  $\gamma/\gamma'$  interface is

associated with an interface dislocation (we observed this for several other dislocations). Similar grooves are observed in the APT measurements, Figure 11d. Even though the dislocations were not directly revealed in APT, it is likely that those grooves are also associated with interface dislocations. Interestingly, the APT measurement presented in Figure 11d does not show local enrichments of chemical elements around the groove, which would point to segregation of certain elements to interface dislocations. Concerning the formation of the grooves they may form as a result of compressive forces exerted on the  $\gamma/\gamma'$  interface due to the presence of dislocations during high temperature exposure. Alternatively, they may result from an increase in  $\gamma'$  volume fraction and associated preferential growth of the  $\gamma'$  phase upon cooling from the high temperature regime. The  $\gamma/\gamma'$  interface appears to propagate towards the  $\gamma$  phase. If the interface dislocations cannot follow this movement they either are incorporated in the  $\gamma'$  phase forming an APB or the interface forms a groove. The latter scenario appears to be energetically favorable. Further work is required to clarify this hypothesis.

#### 4.4. Importance of Cooling Rate

It is quite common to perform creep experiments or homogenization heat treatments at high temperatures and investigate the microstructure at ambient temperature. One has to be careful when interpreting elementary high temperature deformation and transformation mechanisms on the basis of microscopic studies at room temperature. Certain microstructural features may be associated with precipitation processes during slow cooling rather than with a homogenization heat treatment or with isothermal creep itself. This may apply to the small spheroidal  $\gamma$  particles, which are present in the  $\gamma'$  phase (Figure 6 (STEM and HRTEM) and Figure 11c (APT)). This may also apply to the small  $\gamma'$  agglomerates in the  $\gamma$  channels after creep, Figure 11d, as was suggested by Reed *et al.*<sup>[31]</sup>

#### 4.5. Chemical Composition of $\gamma$ and $\gamma'$ Phase, Complementary Methods

The results obtained in the present study clearly show that the elements Al, Ta, and Ti segregate to the  $\gamma'$  cubes while the elements Co, Cr, Re, and W partition to the  $\gamma$  channels. This can be qualitatively observed using EDX in the TEM, Figure 7. A quantitative evaluation of EDX data suffers from the fact that the d-shell elements Ta, W, and Re show overlapping energy spectra of characteristic X-ray energies. This explains why the Ta data in Figure 8 do not reflect the observed trends. APT, which yields more accurate data due to its high spatial ( $\leq 1$  nm) and mass ( $m/\Delta m \geq 1000$ ) resolution, confirms these trends quantitatively, Table 6. At the same time, no significant difference in phase compositions was found between D and ID regions, i.e., dendrite-scale segregations are manifested in the volume fractions of  $\gamma$  and  $\gamma'$  phases. In the present work, we have shown that a combination of macroscopic EPMA results and microscopic APT results enables accurate

determination of  $\gamma'$  volume fractions in dendrites ( $f_{\gamma'} = 72\%$ ) and ID regions ( $f_{\gamma'} = 77\%$ ).

### 5. Summary and Conclusions

In the present work, we investigate laboratory plates of the cast single crystal Ni-base superalloy ERBO1. We use chemical, microstructural, and mechanical methods to characterize the macroscopic homogeneity of the heat treated plate and to identify microstructural and chemical differences between the elements, which characterize the large scale (D and ID regions) and small scale heterogeneities ( $\gamma'$  cubes and  $\gamma$  channels). From the results obtained in the present study, the following conclusions can be drawn:

- 1) The dendritic solidification of single crystal Ni-base superalloys introduces a large scale microstructural heterogeneity into the microstructures where D and ID regions can be clearly distinguished even after extensive homogenization heat treatments. Dendrite spacings are distributed quantities with a large scatter (e.g., 100–900  $\mu\text{m}$ ). Elements like Re, Co, and Cr partition to the D while ID regions show higher concentrations of Al, Ta, and Ti. In modern single crystal technology, it is important to be able to distinguish between local properties of dendrites and ID regions.
- 2) Chemical and mechanical properties of a Ni-base single crystal superalloy plate appear homogeneous, when they are determined from volumes with dimensions,  $d_{\text{vol}}$ , exceeding the length scale of the large scale microstructural heterogeneity associated with the elements of the cast microstructure  $d_{\text{lmh}}$ , i.e., when the specimen size is significantly larger than the dendrite spacing ( $d_{\text{vol}} \gg d_{\text{lmh}}$ ). For the plate studied in this work, this holds for measurements of the average chemical composition as well as for elastic constants and local creep properties.
- 3) In the  $\gamma/\gamma'$  microstructure, elements like Al, Ti, and Ta partition to the  $\gamma'$  cubes while  $\gamma$  channels are richer in Re, W, Co, Cr, and Mo. This can be seen using TEM and APT. APT yields more reliable local data, and, in addition, provides 3D information on the spatial distribution of the elements in the microstructure. High spatial resolution APT results can be combined with EPMA results, which average over characteristic D and ID regions to obtain a good estimate of the  $\gamma'$  volume fractions in D and ID regions.
- 4) The results obtained in the present study show that HR-TEM and APT can help to assess the physical nature of  $\gamma/\gamma'$  interfaces and the role of  $\gamma/\gamma'$  interface dislocations during high temperature plasticity and during the directional coarsening of  $\gamma'$  particles. Grooves at the other way around  $\gamma/\gamma'$  interfaces were observed with a concave radius of 5 nm, which are associated with the presence of interface dislocations. No segregation of specific alloy elements to the groove region was observed. Further work on samples subjected to different creep conditions (stress/

temperature) is required to clarify whether or not interface dislocations contribute to rafting.

- 5) When assessing microstructures of Ni-base single crystal superalloys it is important to distinguish between features, which represent high temperature phenomena and other features of the microstructure, which are associated with slow cooling. Small  $\gamma$  particles in the  $\gamma'$  cubes and small  $\gamma'$  clusters in the  $\gamma$  channels may well be associated with slow cooling from creep temperatures. Further work is required to clarify this point.

### 6. Appendix – Materials Designation ERBO

The present work was performed as a joint effort from SFB/TR 103 projects. Our material designations “ERBO” consist of the two starting letters from Erlangen and Bochum, the locations of the Friedrich-Alexander Universität Erlangen-Nürnberg and the Ruhr-Universität Bochum collaborating in the DFG funded research center SFB/TR 103. The number 1 after ERBO (ERBO/1) refers to the chemical composition (1 – representing a composition close to CMSX-4). Any further ERBO alloy with different chemical composition will be identified by a different number (e.g., 2 – leaner composition featuring less refractory elements). The letters A, B, and C refer to post cast treatments (A – as cast condition, B – solution-treated condition, C – fully heat-treated condition). The following number 1 (here in bold) as in ERBO/1C-1 refers to the specific master melt.

Received: March 19, 2014

Final Version: June 1, 2014

- [1] F. L. Versnyder, M. E. Shank, *Mater. Sci. Eng.* **1979**, 6, 213.
- [2] G. W. Meetham, *The Development of Gas Turbine Materials*, Applied Science Publishers, London, UK **1981**.
- [3] M. McLean, *Directionally Solidified Materials for High Temperature Service*, The Metals Society, London, UK **1983**.
- [4] J. Lacaze, A. Hazotte, *Textures Microstruct.* **1990**, 13, 1.
- [5] R. C. Reed, *The Superalloys: Fundamentals and Applications*, Cambridge University Press, Cambridge, UK **2006**.
- [6] R. Bürgel, H. J. Maier, T. Niendorf, *Handbuch Hochtemperatur-Werkstofftechnik*, Vieweg+Teubner Verlag, Wiesbaden, Germany **2011**.
- [7] M. Durand-Charre, *The Microstructure of Superalloys*, CRC Press LLC, Florida, US **1997**.
- [8] A. Epishin, T. Link, U. Brückner, P. D. Portella, *Acta Mater.* **2001**, 49, 4017.
- [9] F. Pyczac, B. Devrient, F. C. Neuner, H. Mughrabi, *Acta Mater.* **2005**, 53, 3879.
- [10] T. Pollock, S. Tin, *J. Propuls. Power* **2006**, 22, 361.
- [11] K. Serin, G. Göbenli, G. Eggeler, *Mater. Sci. Eng. A* **2004**, 387–389, 133.

- [12] A. Migliori, T. W. Darling, J. P. Baiardo, F. Freibert, *Handbook of Elastic Properties of Solids, Liquids and Gases*, Vol. 1, (Eds: A. G. Every, W. Sachse), Elsevier, New York, USA **2001**.
- [13] G. Mälzer, R. W. Hayes, T. Mack, G. Eggeler, *Metall. Mater. Trans. A* **2007**, 38, 314.
- [14] D. Peter, F. Otto, T. Depka, P. Nörtershäuser, G. Eggeler, *Matwiss. Wtech.* **2011**, 42, 493.
- [15] F. Ernst, M. Rühle, *High Resolution Imaging and Spectroscopy of Materials*, Springer-Verlag, Berlin/Heidelberg, Germany **2003**.
- [16] B. Fultz, J. M. Howe, *Transmission Electron Microscopy and Diffractometry of Materials*, Springer-Verlag, Berlin/Heidelberg, Germany **2008**.
- [17] T. F. Kelly, D. J. Larson, *Annu. Rev. Mater. Res.* **2012**, 42, 1.
- [18] K. Thompson, D. Lawrence, D. J. Larson, J. D. Olson, T. F. Kelly, B. Gorman, *Ultramicroscopy* **2007**, 107, 131.
- [19] L. Agudo Jacome, P. Nörtershäuser, J. K. Heyer, A. Lahni, J. Frenzel, A. Dlouhy, C. Somsen, G. Eggeler, *Acta Mater.* **2013**, 61, 2926.
- [20] B. Gault, M. Moody, J. Cairney, S. Ringer, *Atom Probe Microscopy*, Springer, New York, USA **2012**.
- [21] N. Warnken, R. C. Reed, *Metall. Mater. Trans. A* **2011**, 42, 1675.
- [22] D. Siebörger, H. Knake, U. Glatzel, *Mater. Sci. Eng. A* **2001**, 298, 26.
- [23] X. Zhang, P. R. Stoddart, J. D. Comins, A. G. Every, *J. Phys. Condens. Matter* **2001**, 13, 2281.
- [24] S. V. Prikhodko, J. D. Carnes, D. G. Isaak, A. J. Ardell, *Metall. Mater. Trans. A* **1999**, 30, 2403.
- [25] O. Hellman, J. Vandenbroucke, J. Rüsing, D. Isheim, D. Seidman, *Microsc. Microanal.* **2000**, 6, 437.
- [26] R. Srinivasan, R. Banerjee, G. B. Viswanathan, J. Tilely, D. M. Dimiduk, H. L. Fraser, *Phys. Rev. Lett.* **2009**, 102, 086101-1.
- [27] N. Wanderka, U. Glatzel, *Mater. Sci. Eng. A* **1995**, 203, 69.
- [28] D. Blavette, A. Bostel, *Acta Metall.* **1984**, 32, 811.
- [29] M. Kolbe, A. Dlouhy, G. Eggeler, *Mater. Sci. Eng. A* **1998**, 246, 133.
- [30] V. A. Vorontsov, L. Kovarik, M. J. Mills, C. M. F. Rae, *Acta Mater.* **2012**, 60, 4866.
- [31] R. C. Reed, D. C. Cox, C. M. F. Rae, *Mater. Sci. Eng. A* **2007**, 448, 88.